High-performance mid wavelength InAs avalanche photodiode using $AlAs_{0.13}Sb_{0.87}$ as multiplication layer

JIANLIANG HUANG[1], CHENGCHENG ZHAO[1], BIYING NIE[1], SHIYU XIE[2,*], DOMINIC C. M. KWAN[2], XIAO MENG[2], YANHUA ZHANG[1], DIANA L. HUFFAKER[2], AND WENQUAN MA[1,*]

[1] The Key Laboratory of Semiconductor Materials Science, Institute of Semiconductors, Chinese Academy of Sciences, Beijing 100083, China and Center of Materials Science and Optoelectronics Engineering, University of Chinese Academy of Sciences, Beijing 100049, China
[2] School of Physics and Astronomy, Cardiff University, Cardiff, UK
[*] Corresponding author: XieS1@cardiff.ac.uk and wqma@semi.ac.cn

Compiled February 11, 2020

We report on a high-performance mid wavelength infrared avalanche photodetector (APD) with separate absorption and multiplication regions. InAs is used as the absorber material and high bandgap $AlAs_{0.13}Sb_{0.87}$ is used as the multiplication material. At room temperature, the APD's peak response wavelength is 3.27 μm and the 50% cutoff wavelength is 3.5 μm. The avalanche gain reaches 13.1 and the responsivity is 8.09 A/W at 3.27 μm when the applied reverse bias voltage is 14.6 V. The measured peak detectivity D* of the device is 2.05×10^9 cm·Hz$^{0.5}$/W at 3.27 μm.

http://dx.doi.org/10.1364/ao.XX.XXXXXX

1. INTRODUCTION

Mid wavelength (MW) infared photodetectors are widely needed in military and civil applications. Currently, commercially available high-performance MW detectors are mainly based on HgCdTe [1], InSb [2] and PbS/PbSe [3] materials. To detect very weak and even single photon signals [4], APD is by far the most widely used device due to its high internal gain. To obtain high performance, it requires a low k to minimize the excess noise of an APD. $k = \beta/\alpha$, where α and β are the impact ionization coefficient of electron and hole, respectively. The lower the k is, the smaller the excess noise factor is [5]. In this respect, HgCdTe is an ideal APD material in the MW range because its k is close to zero [6]. However, this material also has some drawbacks in terms of APD application. For instance, HgCdTe material suffer from the so-called composition nonuniformity problem. Moreover, CdZnTe substrate for high-performance APD is of high cost and its large size growth is still a challenge. Another ideal material for MW APD is InAs [7]. On the one hand, its bandgap is in the MW range and its value is about 0.41 eV at 77 K and is 0.35 eV at 300 K. On the other hand, it has been reported that its k is also very close to zero [8, 9] and it can achieve a sole electron multiplication with a very small excess noise factor [10]. In spite of these positive features, there are still some hurdles to overcome. Firstly, a large electric field, which is required to achieve high gain, may cause high tunneling dark current in this narrow bandgap material. Secondly, to realize a high internal gain, the thickness of InAs APD should be as thick as 10 μm [4, 9] and the background carrier concentration should be as low as 6×10^{14} cm^{-3} [11, 12]. This poses a serious challenge for the state-of-the-art growth technique. In addition, most of the MW APDs mentioned above need cryogenic cooling to achieve high performance and this definitely increases the detector weight and cost.

In this paper, we report on a MW APD with separate absorption and multiplication regions. InAs is used as the absorber material and high bandgap $AlAs_{0.13}Sb_{0.87}$ is used as the multiplication material. The APD is of high performance. At room temperature, the APD's avalanche gain reaches 13.1 and the responsivity is 8.09 A/W at the peak response wavelength of 3.27 μm when the applied reverse bias voltage is 14.6 V. The shot noise limited detectivity D* of the device is 1.42×10^{10} cm·Hz$^{0.5}$/W at the peak response wavelength while the measured peak D* is 2.05×10^9 cm·Hz$^{0.5}$/W. It is analyzed that the APD's avalanche gain is mainly from AlAsSb rather than InAs. However, when increasing the reverse bias voltage, the InAs's contribution to the avalanche process is increased.

2. DESIGN AND DEVICE FABRICATION

Table. 1 shows the designed APD structure. The design uses separate absorption and multiplication regions and InAs is used as the absorber material and high bandgap AlAsSb is used as the multiplication material. The AlAsSb material, which can be lattice-matched to InAs by tuning the Sb composition, has a large indirect bandgap of 2.035 eV [13]. Therefore, AlAsSb can be used to block the tunneling dark current [14, 15]. It has been demonstrated that $AlAs_{0.56}Sb_{0.44}$ has a large difference between α and β with the k of only about 0.005 [16–18]. This low k is ascribed to the low β because of high phonon scattering rates and large hole effective mass associated with the large Sb composition [19]. Therefore, AlAsSb can be an ideal multiplication material for APD based on the assumption that it has a similar low excess noise performance as that of $AlAs_{0.56}Sb_{0.44}$ lattice-matched to InP. By using the design with separate absorption and multiplication regions, the APD's thickness can

Table 1. Details of the device structure

Material	Design		Modelled	
	Thickness (μm)	Doping (cm^{-3})	Thickness (μm)	Doping (cm^{-3})
InAs	0.5	2.0e18(P)	/	2.0e18
InAs	2.0	undoped	2.0	1.5e16
AlAsSb	0.5	undoped	0.5	1.5e16
InAs	0.8	2.0e18(N)	/	2.0e18
N+ InAs Substrate				

be decreased a lot. Specifically, along the growth direction, the bottom n type contact region is a 0.8 μm thick InAs layer doped to 2×10^{18} cm^{-3} using Si; the avalanche multiplication region is a 0.5 μm thick unintentionally doped AlAsSb layer; the APD absorber is a 2.0 μm thick InAs layer. Finally, the top p type contact region is a 0.5 μm thick InAs layer doped to 2×10^{18} cm^{-3} using Be.

The sample is grown on an epi-ready S-doped InAs (001) substrate by molecular beam epitaxy using As_2 and Sb_2. The substrate is first heated to 500 °C to desorp the native oxide. Then, the substrate is cooled down to 450 °C to grow the designed structure. After growth, the as-grown sample is processed into square mesas with the width ranging from 200 to 500 μm by photolithography and wet chemical etching. The mesa structure is not surface-passivated. Ti (100 nm)/Au (300 nm) alloy is used as both the p and n type Ohmic contact metal.

3. RESULTS AND DISCUSSION

The as-grown sample is characterized by high resolution x-ray diffraction (XRD) measurement with the ω-2θ scan around the InAs (004) reflection using an open detector, as shown in Fig. S1. The full width at high maximum of the XRD AlAsSb (004) peak is about 150 arcsec. The AlAsSb (004) peak is at the low angle side of the InAs (004) substrate peak and this indicates a compressive strain. The strain is calculated to be about 1.1×10^{-3} from the spacing between the InAs substrate peak and the AlAsSb peak. Assuming a coherent growth, the As and Sb mole fraction of the AlAsSb layer is calculated to be 13% and 87%, respectively, which is very close to our design of $AlAs_{0.15}Sb_{0.85}$. The carrier concentration of different layers is measured by the capacitance-voltage (C-V) profiling and Fig. 1(a) shows the result at room temperature. The obtained residual carrier concentration is 1.5×10^{16} cm^{-3} both for the InAs absorber layer and the AlAsSb multiplication layer. The carrier concentration value of different layers is also shown in Table. 1.

Fig. 2(a) shows the dark current curves of a device with mesa size of 400×400 μm^2 for the temperature range from 77 to 300 K. At 77 K, when the reverse bias voltage is smaller than about 10.5 V, the dark current stays nearly unchanged, which is dominated by the background-induced photocurrent owing to insufficient shielding. When the applied reverse bias voltage is larger than 10.5 V, the dark current increases exponentially. By fitting the dark current curve for the reverse bias voltage between 10.5 and 18 V [see Fig. 2(b)], it is found that this exponential increase of the dark current is induced by the band-to-band tunneling current in the InAs material and no avalanche breakdown behavior is observed in our device. The onset of the tunneling current starts at the reverse voltage $\geq$ 10 V, corresponding to the peak electric field of 68 kV/cm.This result suggests that, if a proper charge sheet layer is included for the future device design, the electric field distribution in the InAs layer may be reduced and thus the band-to-band tunneling current can be further reduced.

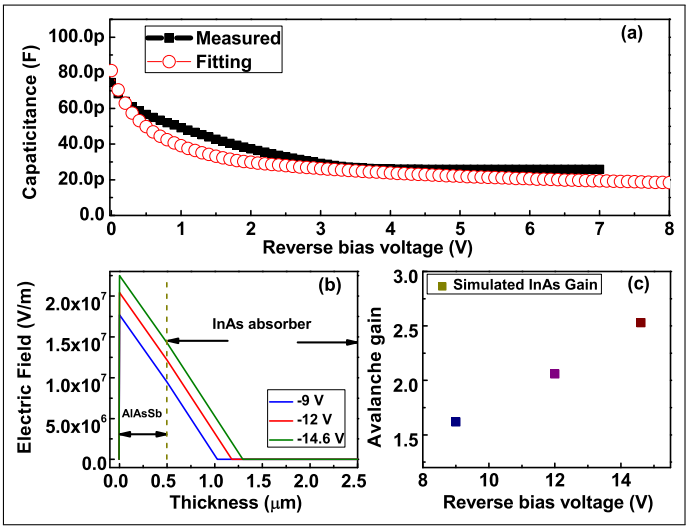

Fig. 1. (a), C-V measured at room temperature withe the fitting. The device size is 400×400 μm^2. (b), Simulated the electric field distribution at different bias voltages. (c), Simulated avalanche gain with respect to the reverse bias voltage.

The activation energy ΔE_{act} can be derived from temperature dependent dark current data. Fig. 3(a) shows the Arrhenius plot of the measured dark current for the temperature range between 77 to 275 K. For the temperature range between 150 to 300 K, ΔE_{act} is 0.33 eV, which equals the value of InAs bandgap at room temperature. This implies that the dark current is dominated by the diffusion current. For the temperature range between 110 and 130 K, ΔE_{act} is calculated to be 0.17 eV, which is about a half of InAs bandgap, and this indicates that the dark current is dominated by the generation-recombination current. When temperature is between 77 to 100 K, the ΔE_{act} is only 38 meV. One possibility is that the dark current for this temperature range may originate from some trap assisted tunneling current. Fig. 3(b) shows the dependence of the extracted ΔE_{act} on the forward bias voltage. By linearly extrapolating the

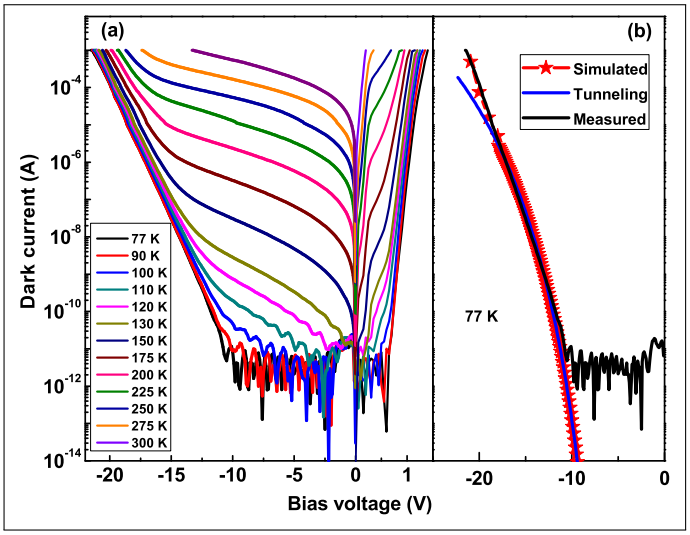

Fig. 2. (a), The dark current curves of a device with mesa area of 400×400 μm^2 for the temperature range from 77 to 300 K. (b), The measured dark current together with the band-to-band tunneling current and the simulated dark current for bias voltage between 10.5 and 18 V.

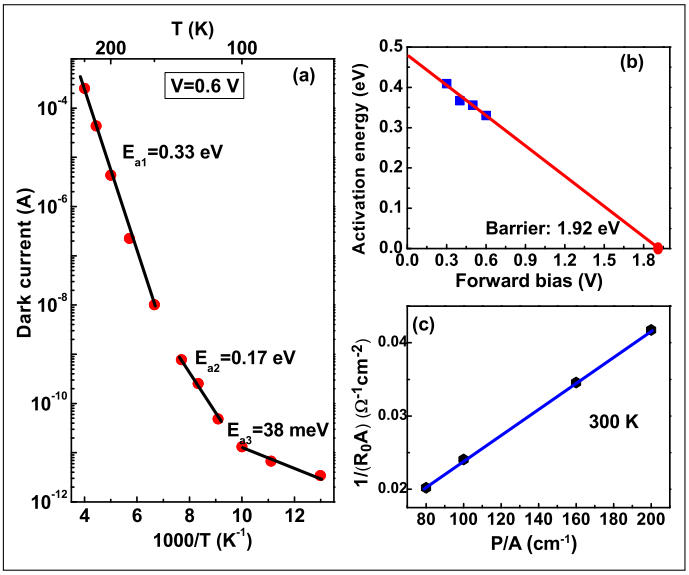

Fig. 3. (a), The Arrhenius plot of the dark current for the temperature range between 77 to 275 K. (b), The activation energy vs. the forward bias voltage. (c), The dependence of the $(1/R_0A)^{-1}$ on the $(p/A)^{-1}$ for different mesa sizes at room temperature.

data to the x-axis, the conduction band offset between InAs and AlAsSb is estimated to be as large as 1.92 eV, which is in agreement with the value of the conduction band offset between InAs and $AlAs_{0.13}Sb_{0.87}$ [13]. This result suggests that, if there is a proper grading layer in between InAs and AlAsSb, the electron transport may be facilitated.

The dark current is measured for variable mesa sizes (500×500, 400×400, 250×250 and 200×200μm^2). Fig. 3(c) is the measured dependence of the $(1/R_0A)^{-1}$ on the $(p/A)^{-1}$ for different mesa sizes at 300 K, where A is the mesa area, p is the mesa perimeter, R_0A is the resistance-and-area product at zero bias, and (p/A) is the perimeter-to-area ratio. From the intercept of the fitting line with the vertical axis, the bulk part of R_0A is calculated to be 200 $\Omega \cdot cm^2$. From the slope of the fitting line, the surface resistivity is obtained to be 5568 $\Omega \cdot cm$. The variable-mesa-size measurements indicate that the surface leakage current is the dominant part of the dark current at room temperature [20]. For example, the surface leakage current contributes 78% of the dark current where the device area is 400×400 μm^2. This is understandable considering that our device is not surface-passivated.

The spectral response of the device is measured by Fourier transform infrared spectroscopy. Then, we measure the blackbody response with the blackbody temperature set at 900 K and use this blackbody response to calibrate the spectral response. In this way, we get the wavelength dependent responsivity. During the measurement, phase-sensitive detection of the photocurrent (chopped blackbody beam and SRS SR830 lock-in amplifier) is employed to minimize the influence of the dark current and the background noise on the photocurrent. Here, we also use a commercial InAs photodiode [21] as a reference to calibrate the optical power and spectra of our system. Fig. 4 shows the measured responsivity under different bias voltages at room temperature. It can be seen that the 50% cut-off wavelength of the device is 3.5 μm, which corresponds to the bandgap of InAs material of 0.35 eV at 300 K. The peak response is at 3.27 μm and the responsivity is 0.62, 1.20 and 8.09 A/W when the applied reverse bias voltage is 7.63, 12.1 and 14.6 V, respectively, which corresponds to the external quantum efficiency of 23.5%, 45.5% and 306.8%, respectively. The responsivity spectrum of the commercial InAs photodiode is also shown in Fig. 4.

The inset of Fig. 5 shows the responsivity with respect to the applied reverse bias voltage for different wavelengths. It can be seen that, when the bias voltage is increased from 0.98 to 7.63 V, the responsivity is increased. This increase is due to the enhanced tunneling probability of photogenerated electrons between InAs and AlAsSb when the bias voltage is increased. When the bias voltage is between 7.63 and 9.28 V, the responsivity is found to be like a plateau. Withe increasing the bias voltage beyond 9.28 V, the responsivity is increased further and this increase is caused by the avalanche effect. Therefore, the bias voltage of 7.63 V is selected as a reference point to calculate the avalanche gain. Fig. 5 is the calculated avalanche gain (M) with respect to the reverse bias voltage for different wavelengths. The avalanche gain reaches to 13.1 at 3.27 μm when the bias voltage is 14.6 V. Here, the maximum gain measured is limited by the high dark current at room temperature, leading to the appearance of the "saturate" avalanche gain. The avalanche gain also can be confirmed from the dark current data. At 77 K, as shown in Fig 2(b), there is a difference between the measured dark current and the simulated InAs band-to-band tunneling current. The simulated band-to-band tunneling current is smaller than the measured dark current when the reverse bias voltage is larger than 18.0 V. Using the same method mentioned above, we can get the multiplication gain at 77 K. Using this multiplication gain, the measured dark current at 77 K can be very well fitted. This indicates the difference is caused by the multiplication effect.

As can be seen from Fig. 5, for a constant bias voltage, the gain stays the same for different wavelengths when the bias voltage is smaller than 14.1 V. However, when the bias voltage is larger than 14.1 V, the gain changes slightly with respect

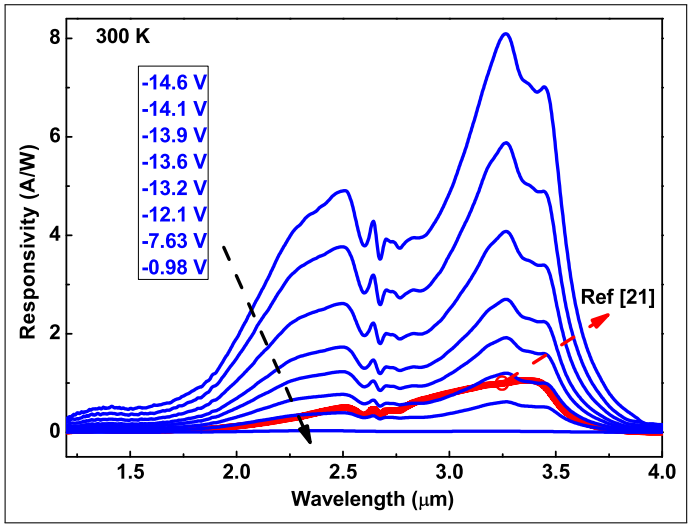

Fig. 4. The measured responsivity under different bias voltages at room temperature. The responsivity of the reference device is also shown.

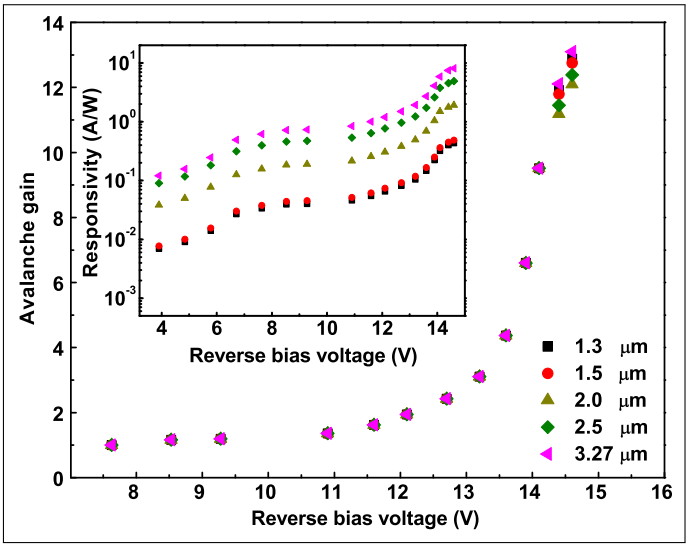

Fig. 5. The avalanche gain with respect to the reverse bias voltage. The inset is the responsivity with respect to the reverse bias voltage for different wavelengths.

to wavelength. For example, the gain is 12.9, 12.8, 12.1, 12.4 and 13.1 for 1.3, 1.5, 2.0, 2.5 and 3.27 μm, respectively. To account for this phenomenon, we should analyze which material, InAs or AlAsSb, the avalanche gain arises from. This can be known by simulating the electron field distribution using the device structure and the carrier density data obtained from the C-V results at room temperature are shown in Fig. 1(b). The simulation was performed assuming the maximum of electric field is at the AlAsSb side. The depletion layer thickness is 1.03, 1.18 and 1.30 μm when the bias voltage is 9, 12 and 14.6 V, respectively. It can be seen that the electric field is predominatly distributed in AlAsSb layer. This implies that the avalanche gain is mainly from AlAsSb layer. In addition, based on the local model, by knowing the electric filed distribution in InAs layer, we can simulate the avalanche gain that the InAs layer contributes to. The result is shown in Fig. 1(c). The avalanche gain from InAs layer is small when the bias voltage is smaller than 14.1 V and it is 1.62 and 2.06 when the bias voltage is 9 and 12 V, respectively. However, the avalanche gain from InAs layer reaches 2.53 when the bias voltage is 14.6 V. This means that, when a large bias voltage is applied, InAs layer also plays a role in the avalanche process, but still, the avalanche effect predominantly comes from AlAsSb rather than InAs. Both the contributions from AlAsSb and InAs make the avalanche gain slightly changed with respect to wavelength under a large bias voltage.

After obtaining the data of the responsivity, the dark current and the gain, the shot noise limited detectivity D* of the device can be calculated by [22]

$$D^\star = \frac{R_i}{\sqrt{2q(J_{ds} + J_{db}M^2F(M)) + \frac{4KT}{R_dA}}}$$

, where R_i is the responsivity, q is the electron charge, J_{ds} is the surface dark current density, J_{db} is the bulk dark current density with gain of one, R_dA is the product of the dynamic resistance and area, K is Boltzmann constant, T is temperature, and M is the avalanche gain. $F(M)$ is the excess noise factor and can be expressed as $F(M) = kM + (2 - \frac{1}{M})(1 - k)$. Here, the k is estimated to be 0.05 according to Ref. [23]. When the M is 10, F(M) is about 2.3. J_{db} is extracted from the dark current data and is about 6.25×10^{-5} A/cm^2. The J_{ds} is roughly equal to 78% of the measured dark current density. The obtained D* is 1.42×10^{10} cm·Hz$^{0.5}$/W at the peak response wavelength of 3.27 μm at 300 K. When the M is 1, the obtained D* is 2.67×10^9 cm·Hz$^{0.5}$/W. The $D^\star$ of the device is also measured at room temperature. The noise spectra (i_n) of the device (bandwidth up to 13.5 KHz) are measured by a spectrum analyzer together with Trans-impedance amplifier [24]. The result of the noise current at different reverse bias voltages is shown in the inset of Fig. 6(a). Using the values of i_n and R_i, the noise equivalent power (NEP) spectra at different reverse bias voltages are obtained according to $NEP = i_n/R_i$, which are shown in Fig.6(a). The experimental $D^\star$ is calculated by $D^\star = A^{1/2}/NEP$ and the result is shown in Fig. 6(b). At 3.27 μm, the measured peak $D^\star$ is 2.05×10^9 cm·Hz$^{0.5}$/W at reverse bias voltage of 14.4 V at 300 K. It can be seen that the measured peak $D^\star$ is about one seventh of the calculated $D^\star$ at M of 10. This might be due to the degradation of device dark current after exposing in the atmosphere environment for more than 2 years. This suggests that a good passivation layer is necessary for our device for long-term application.

This APD's performance is very encouraging. We can compare it with some of the state-of-the-art commercial and reported MW APDs. When the gain is one, the responsivity of our APD is 0.62 A/W, which is smaller than that of Judson [25] and Hamamatsu InAs APD [26]. In particular, it is smaller than the result of the InAs APD reported by the Sheffield group [22], which may be the best result reported. However, when the bias voltage is increased to 14.6 V, our APD's responsivity reaches to 8.09 A/W with the gain of 13.1, which is already larger than that of the two commercial InAs APDs but is still smaller than that of the APD reported by the Sheffield group. The gain of the Sheffield InAs APD can be as large as 200 and the responsivity can be larger than 300 A/W [27]. However, the thickness of the Sheffield InAs APD is 8 μm and is much thicker than ours. Moreover, that device's performance requires the background carrier density as low as 6×10^{14} cm^{-3}. Both the large device thickness and low background carrier density

pose a challenge for most of the present growth techniques. In terms of the detectivity, our APD is comparable to the three InAs APDs mentioned above. We should mention that there is still large room to enhance the APD's performance by effectively surface-passivating the device and by optimizing the device design with some of them like the charge sheet layer and the grading layer schemes mentioned above.

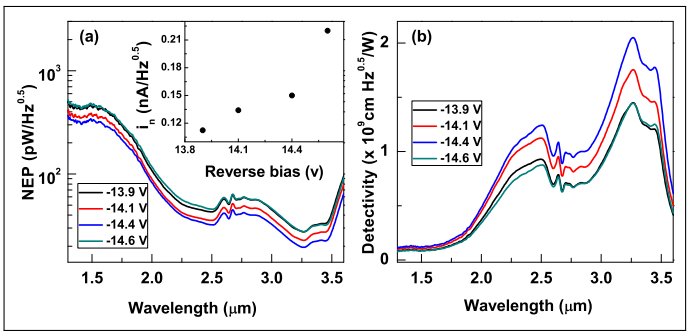

Fig. 6. (a), The measured NEP of the device with respect to wavelength at different reverse bias voltages with the inset showing the measured noise current. (b), The corresponding $D^{\star}$ with respect to wavelength. The device size is 400×400 μm^2.

4. CONCLUSION

We have demonstrated a high-performance MW APD with separate absorption and multiplication regions. At room temperature, the avalanche gain reaches 13.1 and the responsivity is 8.09 A/W at the peak response wavelength of 3.27 μm when the applied reverse bias voltage is 14.6 V. The measured peak detectivity D* of the device is 2.05×10^9 cm·Hz$^{0.5}$/W at 3.27 μm. Our work may provide a new design method to achieve high-performance APD with reduced device thickness.

5. ACKNOWLEDGMENTS

This work is supported in part by The National Key R&D Program of China 2017YFA0303400 and China's NSF Programs 61874103, 61774149, and 61674142.

Disclosures: The authors declare no conflicts of interest.

REFERENCES

1. J. Beck, T. Welch, P. Mitra, K. Reiff, X. Sun, and J. Abshire, "A highly sensitive multi-element HgCdTe e-APD detector for ipda lidar applications," J. Electron. Mater. **43**, 2970–2977 (2014).
2. J. Abautret, J. P. Perez, A. Evirgen, J. Rothman, A. Cordat, and P. Christol, "Characterization of midwave infrared InSb avalanche photodiode," J. Appl. Phys. **117**, 244502 (2015).
3. A. Rogalski, "Recent progress in infrared detector technologies," Infrared Phys. Technol. **54**, 136–154 (2010).
4. C. H. Tan, A. Velichko, and L. W. L. J. S. Ng, "Few-photon detection using InAs avalanche photodiodes," Opt. Express **27**, 5835 (2019).
5. R. J. McIntyre, "Multiplication noise in uniform avalanche diodes," IEEE Trans. Electron Devices **13**, 164–168 (1966).
6. J. Beck, C. Wan, M. Kinch, J. Robinson, P. Mitra, R. Scritchfield, F. Ma, and J. Campbell, "The HgCdTe electron avalanche photodiode," J. Electron. Mater. **35**, 1166–1173 (2006).
7. W. L. Sun, Z. W. Lu, X. G. Zheng, J. C. Campbell, S. J. Maddox, H. P. Nair, and S. R. Bank, "High-gain InAs avalanche photodiodes," IEEE J. Quantum Electron. **49**, 154–161 (2013).
8. A. R. J. Marshall, C. H. Tan, M. J. Steer, and J. P. R. David, "Electron dominated impact ionization and avalanche gain characteristics in InAs photodiodes," Appl. Phys. Lett. **93**, 111107 (2008).
9. A. R. J. Marshall, J. P. R. David, C. H. Tan, and M. J. Steer, "Impact ionization in InAs electron avalanche photodiode," IEEE Trans. Electron Devices **57**, 2631–2638 (2010).
10. A. R. J. Marshall, C. H. Tan, M. J. Steer, and J. P. R. David, "Extremely low excess noise in InAs electron avalanche photodiodes," IEEE Photonics Techn. Lett. **21**, 866 (2009).
11. P. J. Ker, A. R. J. Marshall, J. P. R. David, and C. H. Tan, "Low noise high responsivity InAs electron avalanche photodiodes for infrared sensing," Phys. Status Solidi C **2**, 310–313 (2012).
12. X. X. Zhou, J. S. Ng, and C. H. Tan, "InAs photodiode for low temperature sensing," Proc. SPIE **9639**, 96390V–1–96390V–7 (2015).
13. I. Vurgaftman, J. R. Meyer, and L. R. Ram-Mohan, "Band parameters for III-V compound semiconductors and their alloys," J. Appl. Lett. **89**, 5815–5875 (2001).
14. W. L. Sun, S. J. Maddox, S. R. Bank, and J. C. Campbell, "Room temperature high-gain InAs/AlAsSb avalanche photodiode," 2014 IEEE Photonics Conf. pp. 350–351 (2014).
15. P. J. Ker, J. P. R. David, and C. H. Tan, "Temperature dependence of gain and excess noise in InAs electron avalanche photodiodes," Opt. Express **20**, 29568 (2012).
16. C. H. Tan, S. Y. Xie, and J. J. Xie, "Low noise avalanche photodiodes incorporating a 40 nm AlAsSb avalanche region," IEEE J. Quantum Electron. **48**, 36 (2016).
17. X. Yi, S. Y. Xie, B. L. Liang, L. W. Lim, X. X. Zhou, M. C. Debnath, D. L. Huffaker, C. H. Tan, and J. P. R. David, "Demonstration of large ionization coefficient ratio in AlAs0.56Sb0.44 lattice matched to inp," Sci. Reports **8**, 9107 (2018).
18. X. Yi, S. Y. Xie, B. L. Liang, L. W. Lim, J. S. Cheong, M. C. Debnath, D. L. Huffaker, C. H. Tan, and J. P. R. David, "Extremely low excess noise and high sensitivity AlAs0.56Sb0.44 avalanche photodiodes," Nat. Photonics **37**, 1166 (2019).
19. M. E. Woodson, M. Ren, S. J. Maddox, Y. J. Chen, S. R. Bank, and J. C. Campbel, "Low-noise AlInAsSb avalanche photodiode," Appl. Phys. Lett. **108**, 081102 (2016).
20. Q. Li, W. Q. Ma, Y. H. Zhang, K. Cui, J. L. Huang, Y. Wei, Y. L. Cao, W. Y. Wang, Y. L. Liu, and P. Jin, "Dark current mechanism of unpassivated mid wavelength type II InAs/GaSb superlattice infrared photodetector," Chin. Sci. Bull. **59**, 3696–3700 (2014).
21. Laser-Components, "InAs photodiodes," Available: https://www.lasercomponents.com/de-en/product/inas-900-3500-nm (2019).
22. J. S. Ng, X. X. Zhou, A. Auckloo, B. White, S. Y. Zhang, A. Krysa, J. P. R. David, and C. H. Tan, "High sensitivity InAs photodiodes for mid-infrared detection," Proc. SPIE **9988**, 99880K (2016).
23. Y. Yuan, A. K. Rockwell, Y. W. Peng, J. Y. Zheng, S. D. March, A. H. Jones, M. Ren, S. R. Bank, and J. C. Campbell, "Comparison of different period digital alloy AlInAsSb avalanche photodiodes," J. lightwave technology **37**, 3647 (2019).
24. M. S. Long, A. Y. Gao, P. Wang, H. Xia, C. Ott, C. Pan, Y. J. Fu, E. F. Liu, X. S. Chen, W. Lu, T. Nilges, J. B. Xu, X. M. Wang, W. D. Hu, and F. Miao, "Room temperature high-detectivity mid-infrared photodetectors based on black arsenic phosphorus," Sci. Adv. **3**, e1700589 (2017).
25. Teledyne-Judson-Technologies, "Indium arsenide detectors," Available: http://www.teledynejudson.com/products/indium-arsenidedetectors (2018).
26. Hamamatsu-Photonics, "InAs photovoltaic detector p10090-01," Available: http://www.hamamatsu.com/jp/en/P10090-01.html. (2018).
27. A. R. J. Marshall, P. J. Ker, A. Krysa, J. P. R. David, and C. H. Tan, "High speed InAs electron avalanche photodiodes overcome the conventional gain-bandwidth product limit," Opt. Express **19**, 23341–23349 (2011).